

## Contents

<a href="#">1 Data used</a>	<a href="#">2</a>
<a href="#">2 Global mask generation and sky estimation</a>	<a href="#">3</a>
<a href="#">3 Mask for photometry in image cutout</a>	<a href="#">6</a>
<a href="#">References</a>	<a href="#">8</a>

## 1. Data used

We intend to use a large galaxy sample of different type and age of galaxies to automatically measure their strength and type of tidal features. In order to identify and measure the low surface brightness features reliably, we construct a sample of nearby galaxies in the region of SDSS Stripe 82, which is superior in the depth of its optical imaging. The Sloan Digital Sky Survey (SDSS; [York et al. \(2000\)](#)) is an imaging and spectroscopic survey of the sky using a widefield 2.5 m telescope ([Gunn et al. \(2006\)](#)) with exposure integrations of 53.9 s. Imaging data was gathered in 5 broad bands, *ugriz*, which span the range from 3000 to 11,000 Å ([Fukugita et al. \(1996\)](#)). In addition to single-epoch data, the SDSS also conducted a deep survey by repeatedly imaging a  $275 \text{ deg}^2$  area along the celestial equator in the south Galactic cap ([Adelman-McCarthy et al. 2007](#); [Annis et al. 2014](#)), known as the Stripe 82 survey ([Jiang et al. 2008](#); [Abazajian et al. 2009](#)).

The Stripe 82 survey roughly spans  $-59^\circ < \text{R.A.} < 60^\circ$  and  $-1.25^\circ < \text{Decl.} < 1.25^\circ$  and was scans approximately 80 times. The multi-epoch data allow the construction of deeper co-added images ([Abazajian et al. 2009](#); [Annis et al. 2014](#); [Jiang et al. 2014](#); [Fliri & Trujillo 2016](#)). Co-addition of these multi-epoch images makes the Stripe 82 image reach about 2 magnitude deeper than the normal SDSS image.

Considering about the aim of our work – exploring the galaxy low surface brightness, we prefer a deeper and higher quality of co-added imaging produced by [Fliri & Trujillo \(2016\)](#), which is known as IAC stripe 82 Legacy project (here after IAC). Original single-pass images are downloaded from the SDSS database. In IAC dataset reduction, characteristics of the background (sky + diffuse light) in individual images are preserved by subtract just a single value for the sky background and do not fit it in 1D or 2D modeling. Using this non-aggressive sky subtraction strategy allows the images to preserve as much as possible the low surface brightness features. This is also one of the major differences to previous reductions of Stripe 82 by [Annis et al. \(2014\)](#) and [Jiang et al. \(2014\)](#), which applied background modeling in their reduction pipelines. To ensure the co-addition have well-defined sky background, the IAC project discard single images with large background values taken under bad observing conditions or during grey to bright times. And they reject images with large variations of the sky background from the stacks. In this way, about 2/3 of full available Stripe 82 data with reasonable seeing and darkness are used. The sky-subtracted and photometrically aligned single-epoch images are stacked in each band. Small sky gradients are treated in the co-adds at high signal-to-noise ratio, after which a set of sky-rectified co-adds are provided in the datasets.

IAC project also released a set of ‘ultra-deep r-band’ co-adds. These so-called ‘rdeep’ frames are created by stacking the co-adds of g, r, i bands. The ‘rdeep’ co-adds reach a 1.08 arcsec seeing. Stripe 82 images are processed into patched of  $0.5^\circ$  times  $0.5^\circ$  in right ascension and declination, with a pixel size

of 0.396 arcsec. The co-adds are calibrated to a common zero-point of 24 magnitude for all bands. In our work we use sky-rectified rdeep-band data to generate source masks for each image frame by ourselves, aiming to give a uniform and reasonable source detection for all bands.

## 2. Global mask generation and sky estimation

In order to generate object mask in Stripe 82 region, we begin by running NoiseChisel ([Akhlaghi & Ichikawa \(2015\)](#)) to detect the objects in the IAC image frame ( $0.5^\circ \times 0.5^\circ$ ). NoiseChisel is a noise-based non-parametric technique for detecting nebulous objects. Contrary to other existing signal based detecting software, NoiseChisel is better in detection or morphological analysis of nebulous objects buried in noise, for example, galaxies that do not generically have a known shape when imaged. Its algorithm for initial detection is sky-independent, so it can reach a very low detection threshold and discover the low-surface brightness flux wing around objects. Then the software subsequently classifies detections as true or false based on their signal-to-noise ratio (S/N) using the surrounding undetected regions as a basis. In this way, NoiseChisel is a better tool to generate complete masks and then to estimate sky level. However, considering about its aggressive strategy in detecting signal-effected pixels, we will turn to use Source Extractor (Source Extractor(SEXtractor, [Bertin & Arnouts \(1996\)](#))) when analysing the tidal features and low surface brightness structures in the galaxy outskirts, to ensure that those key features are not masked or ignored. So in our work, we separately generate global mask for calculating the sky, and local mask for running photometry.

Aiming at reasonably masking flux-effected pixels in image tiles as complete and correct as possible, we detect sources in the r-deep band, a deep  $g + r + i$  combined image provided by the IAC Stripe82 survey. The reason we use 'rdeep' image frames is to generate global mask that are appropriate for the g, r, i bands simultaneously. Detectable sources in single g, r, i band-pass are also detected in rdeep band and are lying in background image with deeper flux limit.

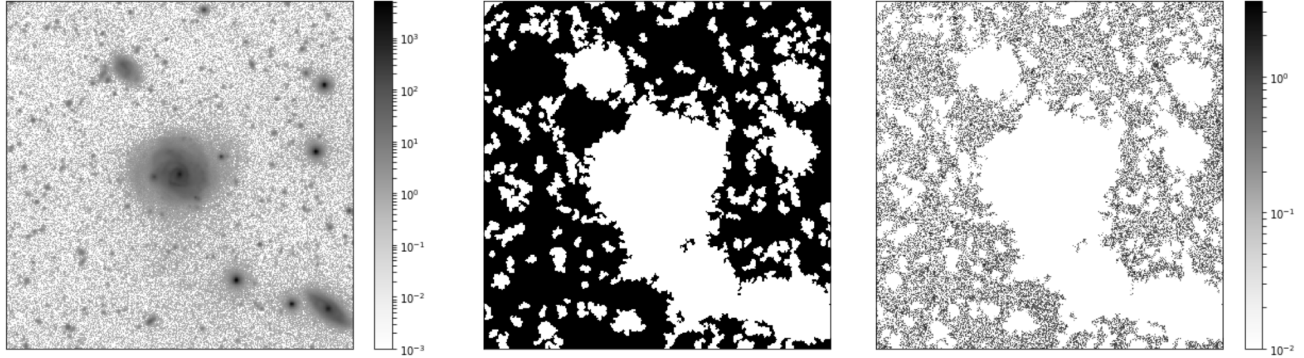


Fig. 1.—: Source mask generated by running NoiseChisel. We do this for the  $0.5^\circ \times 0.5^\circ$  image tile. Figure shown here is a zoomed-in cutout region. *left*: image cutout with length of side equals to 198 arcsec; *middle*: mask for this cutout generated by NoiseChisel *right*: residual sky image.

It is indicated in the completeness simulation in Fliri & Trujillo (2016) that, by applying detection threshold of  $1.74\sigma$  and minimum detection area of 3 connected pixels in SExtractor (Bertin & Arnouts (1996)), the point source recovery fraction in the *ugriz* bands reaches a 50 per cent completeness limit of 24.2, 25.2, 24.7, 24.3 and 23 magnitude respectively. Extended objects having different profile shapes and effective radii are also added to the co-added images and deriving the recovery fraction. They reach average  $\mu_e \sim 25.5 \text{ mag/arcsec}^2$  at the 50 percent completeness level in the r band. The 50 per cent completeness values for the other bands are (25, 26, 25, 24)  $\text{mag/arcsec}^2$  in (u, g, i, z).

We re-perform completeness simulations for point sources and derive the recovery fractions in the ‘rdeep’ co-adds (described above). In our simulation results, we find that our recovery reach a 50% completeness of 25.7 magnitude in ‘rdeep’ band. Although the magnitude in stacking ‘rdeep’ band is not real brightness, but the flux lower limit of detection is deeper than other normal bands and can give valuable insights into low surface brightness features.

Based on the source-masked sky pixels, we estimate the depth and mean value of the sky in each image tile and write them in the header of Stripe 82 image tiles. To sample the sky with appropriate bins, we did tests with a range of sample size. The size of the binning box should be chosen large enough to allow a robust measure of the median, but small enough to be affected by gradients in the sky background. We find that a sample size of 26 pixels ( $\sim 10 \text{ arcsec}$ ) can give a convergent sky rms variations (Fig. 2). According to the results of our experiments, we sample the sky by randomly placing 10000  $26 \times 26$  pix square boxes in the sky area. The fraction of unmasked pixels in each box should be more than 90%. This step binned the sky into square boxes with relative stable sky rms variation (Li et al. (2011)).

Measuring the median value of the count rates (DN) in each square box ( $10'' \times 10''$ , around  $10 \times FWHM$ ), clipping them iteratively at  $3\sigma$  yields the sky mean value and its rms. The surface brightness depth of the ‘rdeep’ images has been estimated using the rms of the images in boxes and corresponds to

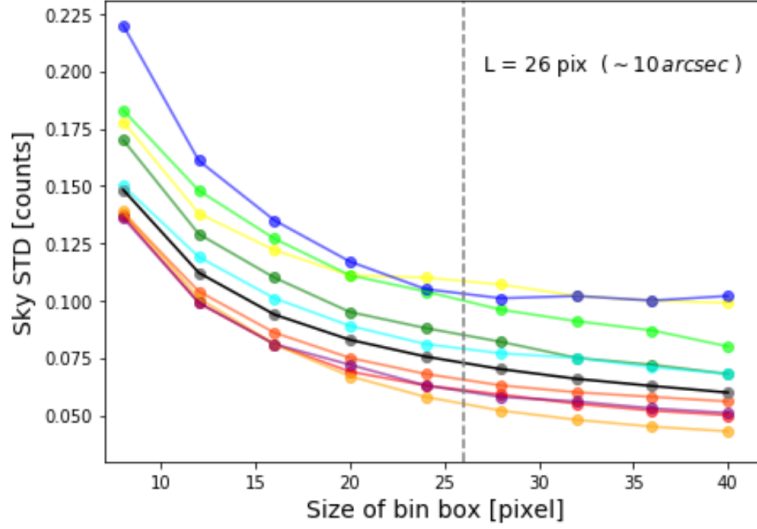


Fig. 2.—: sky std vs. side length(in unit of pixel) to bin pixels. We test it in different position of the IAC r-band image presented as different colors of lines in the figure. Grey vertical line shows that with a size of box larger than that, the variation of sky STD becomes flat approximately. In our work, we use 26 pixels as the side length of every bin box.

$3\sigma$  detections.

Many works has probed the sky rms variations by stacking multiple bands together (van Dokkum 2005; Tal et al. 2009; Atkinson et al. 2013). The photometric calibration is invalid anymore for the averaged  $g + r + i$  coadded band, so the stacks does not have a standard photometric zero-point. Here the definition of an AB magnitude is used to backtrack an equivalent zero point (Atkinson et al. (2013)). We calculated the AB magnitude limit of surface brightness in ‘rdeep’ (deep  $g + r + i$  stacked image) by formula (Roman et al. (2019)):

$$\mu_{lim}(3\sigma) = -2.5 \times \log_{10}\left(\frac{3\sigma}{pix \times pix}\right) + ZP \quad (1)$$

where the zero-point (ZP) magnitude in all bands are calibrated into 28.3291 mag. Pixel size is 0.396 arcsec. As an example, the sky information for image tile ‘f1123\_rdeep.rec.fits’ is shown in figure 3. We derived its smoothed pixel mean -0.0015 DN and sky rms variation  $\sigma_{<gri>} = 0.042$ . So the surface brightness limit for ‘rdeep’ band is  $\mu'_{<gri>,lim} = 28.56$  ‘mag’ (by eq.(1)). Utilizing the mask generated via ‘rdeep’ tile onto u, g, r, i, z-band of the same region, we derived the image surface brightness limit in those bands of  $\mu_{u,lim} = 27.52 \text{ mag/arcsec}^2$ ,  $\mu_{g,lim} = 28.35 \text{ mag/arcsec}^2$ ,  $\mu_{r,lim} = 27.81 \text{ mag/arcsec}^2$ ,  $\mu_{i,lim} = 27.26 \text{ mag/arcsec}^2$ ,  $\mu_{z,lim} = 26.18 \text{ mag/arcsec}^2$  respectively. It is worth noting that the estimated SB limit is strongly dependent on the binning scale. Traditionally, an angular scale of  $10 \times 10$  arcseconds boxes are used as representative of the typical extended source when exploring nearby galaxies, assuming that the sky noise are normally distributed. However, the distribution of realistic sky noise fluctuated

from position to position, e.g. having gradient sometimes. So a shallower limiting depth are usually derived when using a uniform binning size on the un-flat sky background.

One may check the distribution of pixel-value in the background image using some statistical parameters. By comparing the statistic median and mean value of the pixel counts number distribution, we ensure that after masking strategies, our background maps are little influenced by sources in it (with pixel value mean  $\approx$  median and very small skewness, see figure 3). Algorithms Skewness is a measure of the asymmetry of the data around the sample mean. A perfect Gaussian distribution has skewness = 0.

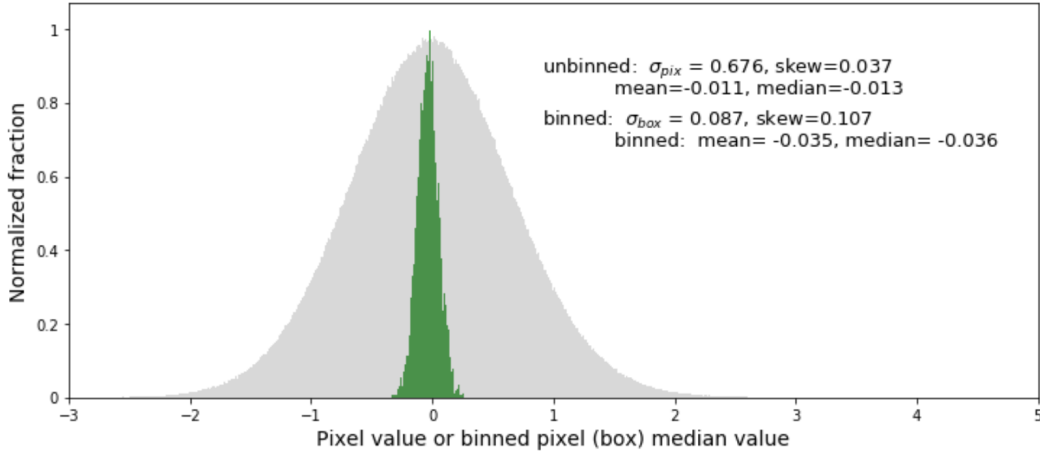


Fig. 3.—: Normalized distribution of original pixel (gray) and median value of binned pixels ( $10'' \times 10''$  square box, green) in source-masked background image of the 3-bands stacked ‘f1123\_rdeep.rec.fits’ tile. The difference between mean and median value is very small, as well as its skewness, see text for details. The realistic SB limit can be calculated via the standard deviation of median value in binned boxes.

### 3. Mask for photometry in image cutout

To perform photometry analysis, we zoom in the local cutout of target object in the coadded *rdeep* image. Then we run SExtractor using setup of lower deblending parameter, e.g. ‘DEBLEND\_MINCONT’=0.001, ‘DETEC\_THRESH’= $3\sigma$  and a criteria of detection pixel area ‘DETECT\_MINAREA’= $5^1$  to detect sources inside image cutoff.

We make elliptical aperture-mask for detected sources (except the target galaxy) according to detection output properties probed by SExtractor. Based on the segmentation image, elliptical apertures are generated based on semi-major-/ semi-minor-axis and ellipticity. Magnification is applied to each aperture according to pixel area above the detection threshold (‘ISOAREA\_IMAGE’) and the Petrosian radius estimated by SExtractor. Petrosian (1976) defined a point in the radial light profile at which the isophote

<sup>1</sup>To get rid of losing the compact bright objects in the real images, the SExtractor manual suggests setting DETECT\_MINAREA to small values (1 – 5) so that the convolution kernel and DETECT-THRESH define the sensitivity.

at that radius was a certain fraction <sup>2</sup> of the average surface brightness within that radius. Such schemes have been discussed many times (e.g., Bershady et al. (1994); Bershady et al. (1998)), and here we adopt the protocol developed by Bershady et al. (2000), which uses twice the radius where  $\eta = 0.2$  to define the total light ( $2R_{\text{petro}}$ ). Inside this radius, we mask only point-like stars ('Class\_star' <sup>3</sup>  $> 0.75$ , Roman et al. (2019)) and other small scale contaminations ('ISOAREA\_IMAGE'  $< 200$ ) to avoid an over-mask to the galaxy substructures, e.g. spiral arms or clumps in nearby galaxies. 1.5 times their Petrosian radius as a magnification to grow the mask is fitted for those objects. Neighbour galaxies near to the target will be manually masked if the target is in a very crowded cluster<sup>4</sup>.

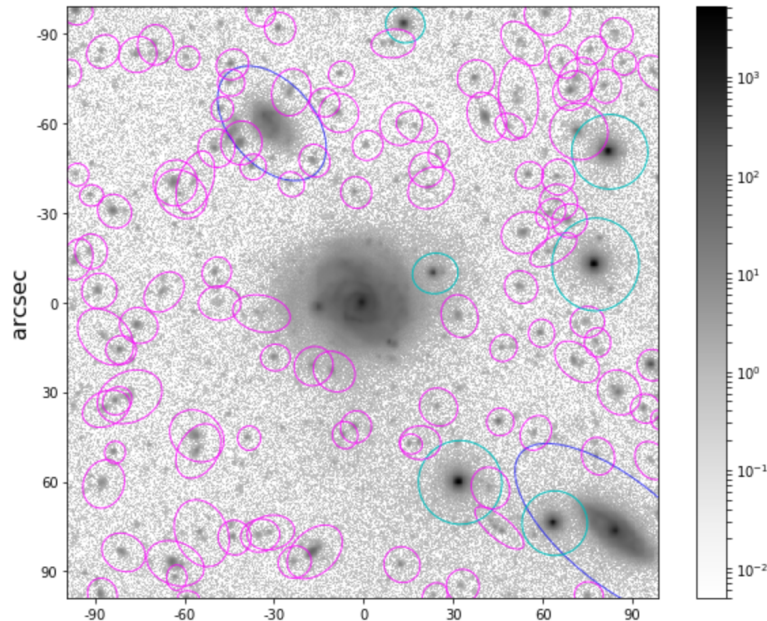


Fig. 4.—: Aperture-mask for local image cutout. The central galaxy is the target object in this cutout. Cyan ellipses mark the aperture-mask for stars; magenta ellipses are apertures grown by 1.5 Petrosian radius for small scale objects; blue ellipses are apertures for extended large scale galaxies. We didn't plot the apertures for galaxies inside  $2R_{\text{petro}}$ , because we will not mask them when doing photometry for our targets. Axes are in unit of pixel.

Meanwhile, we mask all detected sources out of this radius. SEXtractor detected sources having 'Class\_star'  $< 0.75$ ) are considered as extended objects. After many times of tests, we find that 0.45 times square root of detected pixel-area<sup>5</sup> of the object ( $r_{\text{isoarea}}$ ) is a better radius to magnify the aperture-mask for point-like sources and saturate stars ( $\text{mag}_r \lesssim 14$ , Fukugita et al. (1996)) with spike feature in the

<sup>2</sup> $\eta(R) = I(R)/\langle I(R) \rangle$ , Kron(1995); in SEXtractor  $\eta$  is 0.2

<sup>3</sup>A neural network star/galaxy separation determined by SEXtractor

<sup>4</sup>One way to pick out the true neighbours beside, but not clumps in target, is to cross match our output catalog with the galaxy catalog generated by IAC. The overlapped sources (except the target) will be masked using ext-magnification ( $0.2r_{\text{isoarea}}$ )describedinthe following.

<sup>5</sup>In other words, 'ISO\_AREA'.



image, while a gain of  $0.2 \times r_{isoarea}$  is appropriate to magnify the aperture-mask of extended sources (except the target one).

Then we combine the ‘inner mask’ generated for foreground stars in region  $r < 2R_{petro}$ , and the ‘outer mask’ for  $r > 2R_{petro}$ , to make a composite mask specially for galaxy photometry and isophotal analysis. Fig.5 illustrates the inner and outer mask, as well as the total mask for image cutout prepared for photometric analysis.

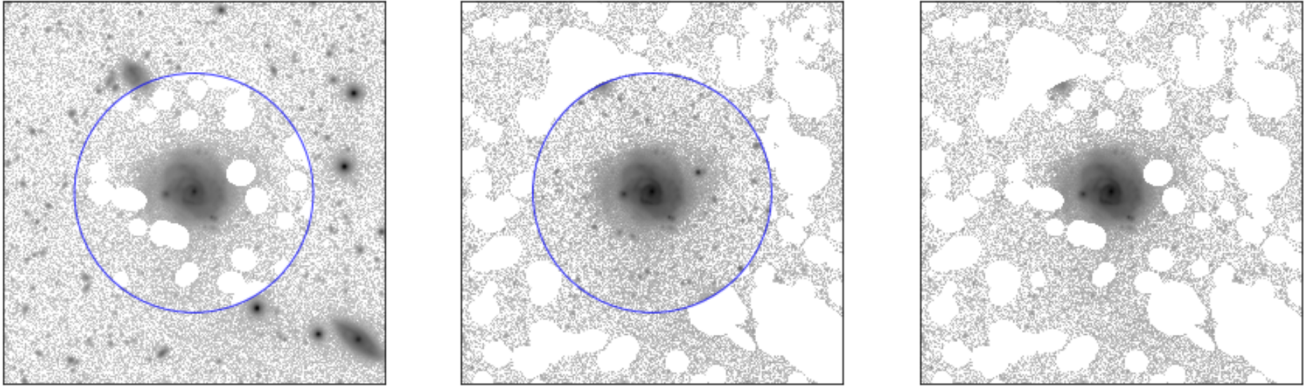


Fig. 5.—: *left*: ‘inner’ mask for stars and other contaminations inside  $r = 2R_{petro}$ ; *middle*: ‘outer’ mask for objects outside  $r = 2R_{petro}$ ; *right*: total mask for running photometry after combination of inner and outer masks.

## REFERENCES

- Abazajian, K. N., Adelman-McCarthy, J. K., Agüeros, M. A., et al. 2009, *ApJS*, 182, 543
- Adelman-McCarthy, J. K., Agüeros, M. A., Allam, S. S., et al. 2007, *ApJS*, 172, 634
- Akhlaghi, M., & Ichikawa, T. 2015, *ApJS*, 220, 1
- Annis, J., Soares-Santos, M., Strauss, M. A., et al. 2014, *ApJ*, 794, 120
- Atkinson, A. M., Abraham, R. G., & Ferguson, A. M. N. 2013, *ApJ*, 765, 28
- Bershady, M. A., Hereld, M., Kron, R. G., et al. 1994, *AJ*, 108, 870
- Bershady, M. A., Jangren, A., & Conselice, C. J. 2000, *AJ*, 119, 2645
- Bershady, M. A., Lowenthal, J. D., & Koo, D. C. 1998, *ApJ*, 505, 50
- Bertin, E., & Arnouts, S. 1996, *A&AS*, 117, 393
- Fliri, J., & Trujillo, I. 2016, *MNRAS*, 456, 1359
- Fukugita, M., Ichikawa, T., Gunn, J. E., et al. 1996, *AJ*, 111, 1748



- Gunn, J. E., Siegmund, W. A., Mannery, E. J., et al. 2006, *AJ*, 131, 2332
- Jiang, L., Fan, X., Annis, J., et al. 2008, *AJ*, 135, 1057
- Jiang, L., Fan, X., Bian, F., et al. 2014, *ApJS*, 213, 12
- Li, Z.-Y., Ho, L. C., Barth, A. J., & Peng, C. Y. 2011, *ApJS*, 197, 22
- Petrosian, V. 1976, *ApJ*, 210, L53
- Roman, J., Trujillo, I., & Montes, M. 2019, *arXiv:1907.00978v1*
- Tal, T., van Dokkum, P. G., Nelan, J., & Bezanson, R. 2009, *AJ*, 138, 1417
- van Dokkum, P. G. 2005, *AJ*, 130, 2647
- York, D. G., Adelman, J., Anderson, Jr., J. E., et al. 2000, *AJ*, 120, 1579